Impact of angle of attack and relative width of V-shaped ribs on the thermo-hydraulic performance of a solar air heater

Hananeh Ghasemi and Leila N. Azadani*

* Corresponding author's email: l.azadani@aut.ac.ir

Department of Chemical Engineering, Amirkabir University of Technology, Tehran, Iran

Abstract:

Solar air heaters offer a low-cost way to convert solar energy into usable heat, but their efficiency is limited by the inherently low heat transfer coefficient of air. To address this limitation, artificial roughness elements such as V-shaped ribs are commonly added to the absorber plate to boost turbulent mixing and improve thermal performance. This study numerically investigates the thermo-hydraulic characteristics of a solar air heater duct equipped with V-shaped ribs by analyzing the combined effects of angle of attack and relative rib width using computational fluid dynamics. The results demonstrate that both thermal performance and flow characteristics are influenced by rib geometry. The Nusselt number reaches its maximum enhancement of 2.8 times that of a smooth duct when using a single V-rib with a relative width of 1 and a 30° angle of attack. However, reducing the relative width results in progressively diminished heat transfer effectiveness. The thermo-hydraulic performance parameter peaks at 1.63 for the optimal relative width of 1 at a 30° angle of attack, indicating the most favorable ratio of Nusselt number enhancement to friction factor increase. These results offer essential guidance for optimizing roughened solar air heater designs, suggesting that a single, properly oriented V-rib offers the most favorable compromise between thermal enhancement and energy efficiency.

Keywords:

Solar air heater, Nusselt number, V-shaped rib, Angle of attack, Relative rib width

1

1. Introduction

Solar energy stands out due to its vast, readily available potential. Harnessing this abundant resource is accomplished primarily through two distinct technologies. The first is photovoltaic cells, which are constructed from semiconductor materials. These cells possess the unique property of generating electricity directly when exposed to sunlight. The second major technology involves solar thermal collectors. These systems feature channels with a specialized absorber plate designed to capture solar radiation. The absorbed heat energy is then transferred to a working fluid, commonly water or air, circulating through these channels.

Focusing specifically on solar thermal systems using air, known as solar air heaters (SAHs), reveals a particular challenge due to the inherently low heat transfer coefficient of air. This property severely limits the ability of air to absorb and transport thermal energy from the absorber plate. To overcome this, two main strategies are employed: passive and active enhancement techniques. A key active method to address this is jet impingement, where high-velocity air streams are directed at the absorber plate to disrupt the boundary layer and significantly enhance heat transfer. The thermo-hydraulic performance of this technique depends critically on the Reynolds number, jet geometry, and configuration [1-3].

In contrast to active methods, passive techniques improve efficiency by modifying the geometry of SAH without external power. A highly effective approach involves adding artificial roughness to the absorber plate. These elements disrupt the laminar airflow, promoting turbulence and enhancing heat transfer. Various geometries, such as discrete cylindrical elements [4], boomerang-shaped elements [5], C-shaped ribs [6], and boot-shaped ribs [7] have been studied. Among these, V-shaped ribs have attracted significant research interest due to their effectiveness.

Key geometric parameters of V-shaped ribs, such as the angle of attack, relative width, relative height, and relative pitch, have been extensively studied. Momin et al. [8] demonstrated that a relative height of 0.034 and an angle of attack of 60° improved the Nusselt number, *Nu*, by a factor of 2.30 compared to a smooth channel. Lanjewar et al. [9] found that W-shaped ribs (V-shaped ribs with a relative width of 2) perform

best at a relative height of 0.03375 and an angle of attack of 30°, achieving a 2.21-fold *Nu* improvement. Furthermore, they found that the W-up orientation (apex facing upstream) achieved higher *Nu* augmentation and a lower friction factor, *f*, than the W-down configuration [10]. Sharma et al. [11] reported optimal performance at a relative pitch of 10, an angle of attack of 60°, and a relative height of 0.033. Under these conditions, *Nu* increased by 1.7 times compared to a smooth absorber plate. Jin et al. [12, 13] found peak performance at a 45° angle of attack, with *Nu* increasing but *THPP* decreasing with relative width. Sharma and Bhargava [14] found that both *Nu* and *f* decrease as the angle of attack increases from 30° to 90°. Kadijani et al. [15] reported maximum *Nu* and *THPP* at a 30° angle of attack, with *THPP* decreasing with relative pitch and *Nu* increasing with the humidity of the inlet air. Salarpour and Azadani [16] showed *Nu* initially improves then declines with rib height for relative widths of 1 and 2, while consistently decreasing for widths of 3 to 5. Pachori et al. [17] found optimal performance at a 60° angle of attack with a relative width of 6, a relative pitch of 8, and a relative height of 0.043. Ghasemi Noureini and Azadani [18] demonstrated that leading edge rib placement yields higher *THPP*.

Beyond continuous ribs, broken V-shaped ribs have also been investigated, with parameters like relative height, pitch, gap distance, gap width, angle of attack, and relative width being analyzed [19-21]. Jin et al. [22] demonstrated that staggered V-shaped ribs significantly outperform continuous ribs, achieving a *THPP* of 2.43 in optimal configurations. Hegde et al. [23] evaluated the performance of SAHs equipped with various V-shaped rib configurations and confirmed that staggered discrete V-ribs delivered the highest thermo-hydraulic efficiency among all tested designs.

The geometric parameters of V-shaped ribs, specifically the angle of attack and relative rib width, have primarily been investigated in isolation in previous studies. These parameters were traditionally examined using a one-variable-at-a-time approach, wherein all other variables were held constant while only one was altered. As a result, the interaction effects between these key parameters have remained largely unknown and unquantified. This gap is addressed in the present study through the application of a full factorial design of experiments, enabling a coordinated analysis of both the angle of attack and relative width

simultaneously. This method allows for the quantification of interaction effects and clarifies how these factors jointly influence thermo-hydraulic performance.

2. Numerical Method

The ANSYS Workbench 19.0 software was used for all simulations. The geometry was created in DesignModeler, the computational grid was generated in Meshing, and the SAH air flow was solved using Fluent.

2-1- Governing Equations

The air flow and heat transfer characteristics within the SAH were investigated numerically using the Reynolds-Averaged Navier-Stokes (RANS) equations. These equations are as follows [24]:

$$\frac{\partial \overline{u}_i}{\partial x_i} = 0 \tag{1}$$

$$\overline{u}_{j} \frac{\partial \overline{u}_{i}}{\partial x_{j}} = -\frac{1}{\rho} \frac{\partial \overline{P}}{\partial x_{i}} + \nu \frac{\partial^{2} \overline{u}_{i}}{\partial x_{j} \partial x_{j}} + \frac{\partial}{\partial x_{j}} \left(-\overrightarrow{u_{i} u_{j}} \right)$$

$$(2)$$

$$\overline{u}_{j} \frac{\partial \overline{T}}{\partial x_{j}} = \alpha \frac{\partial^{2} \overline{T}}{\partial x_{j} \partial x_{j}} + \frac{\partial}{\partial x_{j}} \left(-\overline{T' u_{j}} \right)$$
(3)

where \overline{u}_i and u_i are the time averaged and fluctuating components of the velocity, \overline{T} and T' are the time averaged and fluctuating components of the temperature, and \overline{P} denotes the time averaged pressure. Fluid properties are density, ρ , kinematic viscosity, ν , and thermal diffusivity, α . The term $-\overline{u_i}$ represents the Reynolds stress, while $-\overline{T'u_j}$ signifies the turbulent heat flux. These are modeled as [24]:

$$-\overline{u_i'} \ u_j' = -2v_T \overline{S}_{ij} - \frac{2}{3} \delta_{ij} k \tag{4}$$

$$-\overline{T'u_j'} = \frac{v_T}{Pr_T} \frac{\partial \overline{T}}{\partial x_j} \tag{5}$$

In this formulation, \overline{S}_{ij} represents the time averaged strain rate tensor, v_T denotes turbulent eddy viscosity, δ_{ij} is the Kronecker delta, k signifies turbulent kinetic energy, and Pr_T is the turbulent Prandtl number. The Reynolds stress and turbulent heat flux are both functions of v_T , which can be modeled through different turbulence closure approaches. To determine v_T , various turbulence models exist. Previous research [17, 18] identifies the RNG $k-\varepsilon$ model as particularly suitable for SAH simulations. Consequently, this study employs the RNG $k-\varepsilon$ model [25].

After solving Eqs. (1-3) for the velocity and temperature fields, the friction factor and Nusselt number were calculated using the following expressions:

$$f = \frac{\Delta P D_h}{2\rho L V^2} \tag{6}$$

where ΔP is the pressure drop across the absorber section of SAH, D_h is the hydraulic diameter of the SAH channel, L denotes the length of the absorber section, and V is the average air velocity in the channel.

The Nusselt number varies along the channel length. The local Nusselt number, Nu_x , is given by:

$$Nu_{x} = \frac{q''D_{h}}{(T_{w} - T_{b})\kappa}$$

$$(7)$$

where q'' is the applied heat flux on the absorber plate, T_w is the local absorber plate temperature, and T_b is the local bulk temperature, defined as the mass-weighted average temperature at each channel cross-section. The average Nusselt number for entire absorber section is then calculate by:

$$Nu = \frac{\int Nu_x dA}{A} \tag{8}$$

where A is the area of the absorber plate.

2-2- Geometry

The SAH channel, illustrated in Fig. 1, is designed as a square duct with a cross-section of 50 mm×50 mm. Consequently, the hydraulic diameter, which serves as the characteristic length, is 50 mm.

The channel is segmented into three distinct sections, including inlet, absorber, and outlet, in accordance with ASHRAE Standard [26]. This standardized design is critical for generating hydrodynamically fully developed flow prior to the absorber section, thereby establishing a consistent and predictable velocity profile for accurate thermal analysis. Furthermore, the outlet section is sufficiently elongated to minimize flow reversal and pressure disturbances at the exit, ensuring that measurements are not adversely affected by boundary effects. The absorber section forms the core of SAH, where heat transfer occurs. Its top wall is a 1 mm thick plate made of aluminum, chosen for its high thermal conductivity. This plate is subjected to a constant uniform heat flux, simulating the thermal input from solar radiation.

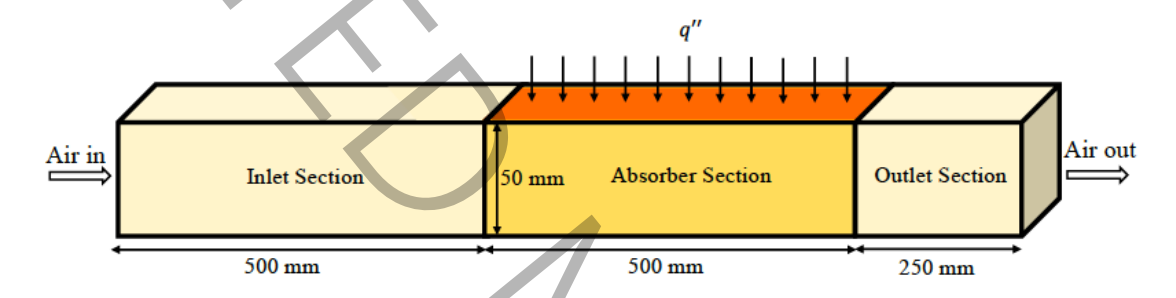


Fig. 1. Geometry of SAH.

Fig. 2 provides a detailed top and side view of the roughened absorber section, illustrating the arrangement of the V-shaped ribs. In Fig. 2(a), a single V-rib spans the entire width of the channel, thus, the rib width (w) is equal to the channel width (H). The key geometric parameter, the relative width, is defined as the ratio H/w. For the configuration in Fig. 2(a), this ratio is 1. Subsequent subfigures demonstrate V-shaped ribs with progressively narrower widths. In Fig. 2(b), the width of a single V-rib is half of the channel width, resulting in a relative width of 2. This pattern continues in Figs. 2(c) and 2(d), where the relative widths are 3 and 4, respectively. Another critical parameter, the angle of attack (α) , which defines the V-orientation relative to the air flow, is annotated in Fig. 2(a). All ribs featured a square cross-section with a consistent height, e, of 5 mm. The center-to-center spacing between consecutive ribs, known as the pitch, e, was fixed at 50 mm for all configurations. A comprehensive analysis was conducted using a full factorial design of experiments. Five angles of attack, 15° , 30° , 45° , 60° , 75° , and 90° , and four relative rib widths, 1, 2, 3, and 4, were tested, resulting in 24 detailed numerical simulations.

An inlet velocity of 4.38 m/s corresponding to the Reynolds number of 15,000 and temperature of 300 K were applied, with 0 Pa gauge pressure at outlet. No-slip conditions were enforced on all channel walls, while thermal conditions consisted of a constant 1000 W/m² heat flux uniformly applied to the absorber plate, with all remaining surfaces treated as adiabatic.

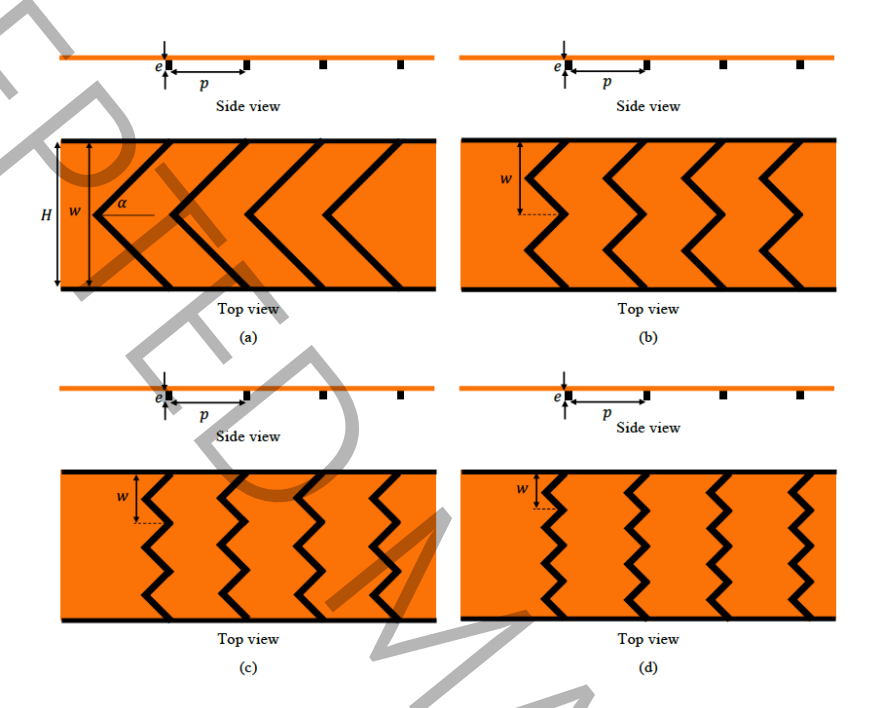


Fig. 2. Geometry of V-shaped ribs used as the roughness, a) H/w=1, b) H/w=2 c) H/w=3, and d) H/w=4.

ANSYS Fluent's finite volume-based solver was implemented to discretize and solve the governing equations. Given the incompressible nature of the air flow within SAH, a pressure-based solver was selected. The pressure-velocity coupling was resolved using the SIMPLE algorithm. A second-order accurate upwind scheme was implemented for spatial discretization of all transport equations. Solution convergence was rigorously monitored, requiring residuals for all variables to fall below 10^{-6} . The analysis assumed constant thermo-physical properties for air as listed in Table 1.

Table 1. Thermo-physical properties of air.

Property	Density	Specific Heat	Thermal Conductivity	Viscosity
	(kg/m^3)	$(J/kg \cdot K)$	(W/m·K)	(kg/m·s)
Air	Air 1.225		0.024	1.789×10 ⁻⁵

2-3-Mesh

A well-structured computational grid is essential for accurate and efficient computational fluid dynamics (CFD) simulations. Mesh resolution critically influences both solution accuracy and computational cost, as overly coarse meshes produce inaccurate results, while excessively refined meshes demand prohibitive computational resources. An optimal mesh density was determined through a grid independence study. Fig. 3 presents the results of this study for a duct with V-shaped ribs of relative width 1 and a 15° angle of attack, showing the variation of Nu with mesh element count. The results indicate that Nu exhibits negligible variation beyond 5.9 million elements. As shown in Table 2, the error between the last two mesh refinements is only 0.16%, confirming the suitability of the 5.9 million element mesh. Similar grid independence studies were performed for all other geometric configurations to ensure consistent resolution. Fig. 4 shows the computational mesh at a relative width of 1 and a 15° angle of attack. A fine tetrahedral mesh was employed near the walls to effectively capture flow gradients and ensure solution accuracy in critical regions. Near-wall resolution was carefully controlled, with y^+ values maintained near unity across all simulations to accurately resolve boundary layer effects.

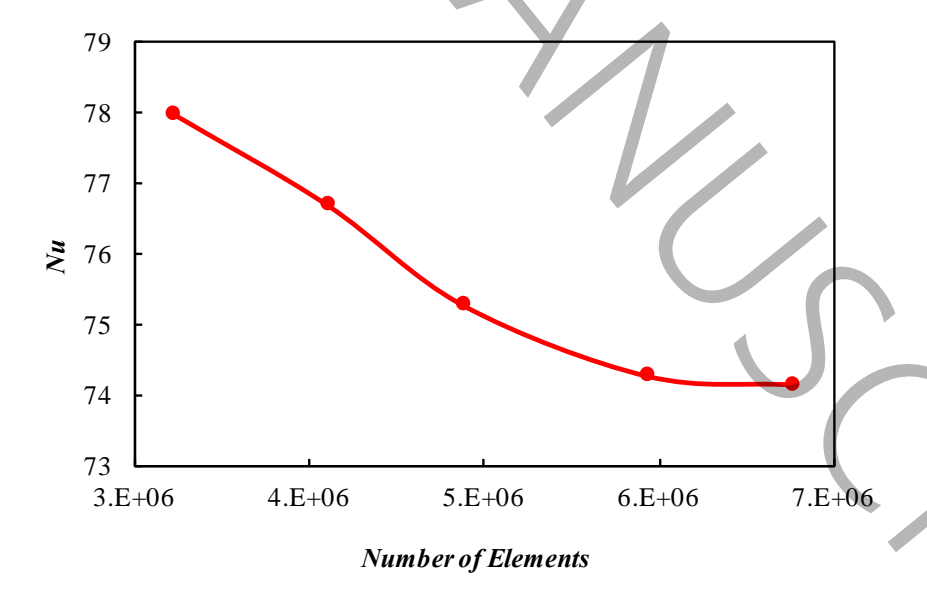


Fig. 3. Mesh independence test for V-shaped ribs at a relative width of 1 and an angle of attack of 15°

Table 2. The Nusselt number and error at different mesh resolutions.

Number of Elements	3,222,062	4,107,424	4,890,503	5,935,794	6,762,643
Nusselt Number	77.98	76.58	75.26	74.27	74.15
Error (%)	-	1.83	1.75	1.33	0.16

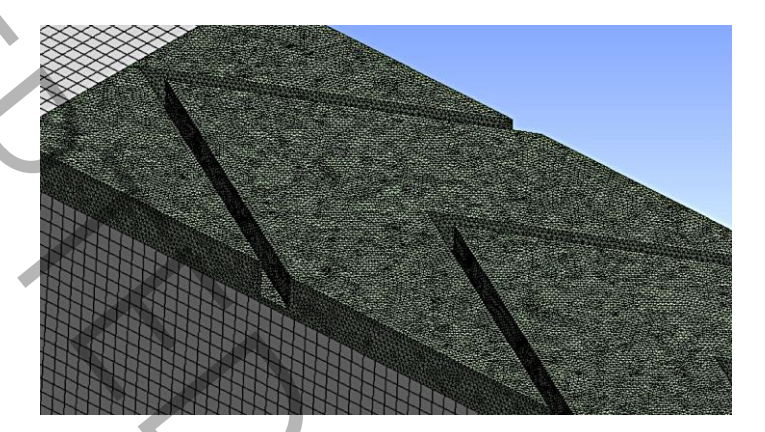


Fig. 4. Distribution of the computational grid at a relative width of 1 and an angle of attack of 15°.

2-4- Validation

Validation, confirming the agreement of CFD simulations with physical reality, is a fundamental requirement. Numerical predictions of both f and Nu were validated against established correlations across multiple Reynolds numbers, Re,. The Blasius equation [27] served as the benchmark for f, while the Dittus-Boelter relation [28] verified heat transfer results. The Blasius and Dittus-Boelter correlations are given by Eqs. (9) and (10):

$$f = 0.085 Re^{-0.25} \tag{9}$$

$$Nu = 0.023Re^{0.8}Pr^{0.4} (10)$$

where Re and Pr are the Reynolds number and Prandtl number defined by:

$$Re = \frac{\rho D_h V}{\mu} \tag{11}$$

$$Pr = \frac{\mu}{\rho\alpha} \tag{12}$$

As shown in Fig. 5, the simulation outputs exhibit excellent agreement with established theoretical models. The calculated friction factors align closely with the Blasius correlation, while the Nusselt numbers correspond well with the Dittus-Boelter correlation. This validation is further supported by the data in Table 3, which confirms that all errors for both parameters are below 12.5%.

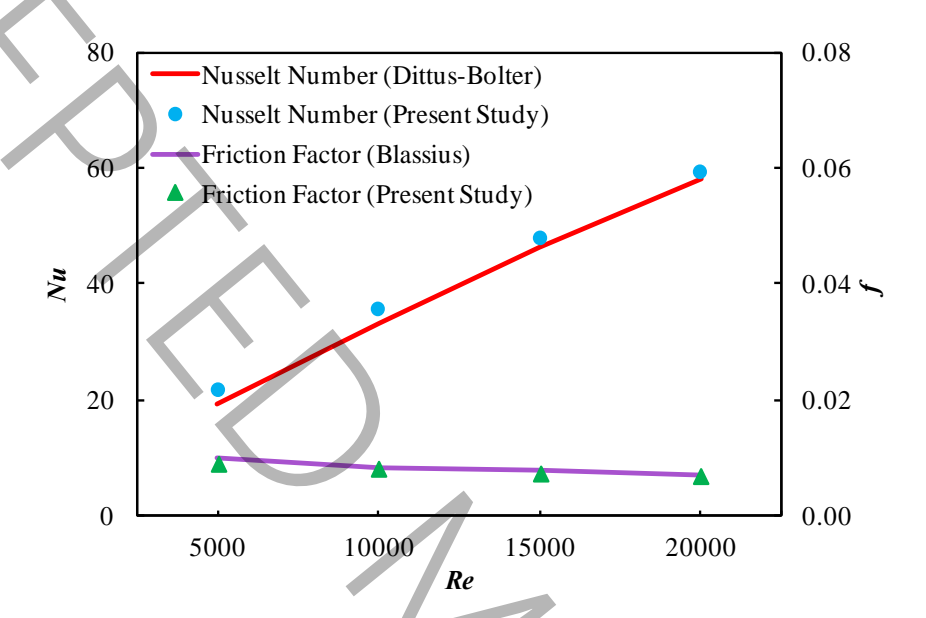


Fig. 5. Validation of f and Nu against established empirical correlations.

Table 3. Comparison of simulated and predicted Nusselt number and friction factor with percentage errors.

Re	Nu	Nu	Error in Nu	f	f	Error in f
	(Dittus-Boelter)	(Simulated)	(%)	(Blasius)	(Simulated)	(%)
5,000	19.15	21.55	12.5	0.0101	0.0090	10.9
10,000	33.34	35.43	6.2	0.0085	0.0080	5.4
15,000	46.12	47.84	3.7	0.0077	0.0072	5.9
20,000	58.06	59.27	2.1	0.0071	0.0068	5.7

3. Results and Discussion

The effect of the angle of attack and relative width on Nu, f, and THPP is discussed in this section. Fig. 6 demonstrates the relationship between Nu and angle of attack for varying relative width. For smaller relative widths, corresponding to fewer and wider V-ribs, Nu peaks at 30°. At this angle, the ribs effectively generate

strong, organized longitudinal vortices. These vortices enhance heat transfer by aggressively sweeping hot fluid away from the surface and entraining cooler fluid from the core flow, significantly thinning the thermal boundary layer. Beyond 30°, the ribs act as more abrupt obstacles, creating large, stable recirculation zones behind them. While these zones contribute to mixing, they primarily trap fluid near the surface, reducing thermal gradients and diminishing heat transfer efficiency despite increased turbulence. In contrast, for larger relative widths, meaning more numerous but narrower V-ribs, *Nu* peaks at a lower angle of 15°. Here, the closely spaced ribs cause early interaction and interference between adjacent vortices. At higher angles, these vortices disrupt each other's coherence, leading to chaotic and dissipated turbulence rather than organized mixing. The lower peak angle mitigates this interference, allowing some beneficial vortex action before breakdown occurs. The relatively small *Nu* variation with increasing relative width indicates a saturation effect in turbulence generation, where additional ribs provide diminishing returns.

Fig. 7 presents the variation of f with angle of attack for different relative widths. It can be seen that for all relative widths, f initially increases with angle of attack, reaches a maximum (typically between 30° - 45°), then decreases at larger angles. This occurs because moderate angles generate strong vortices and flow

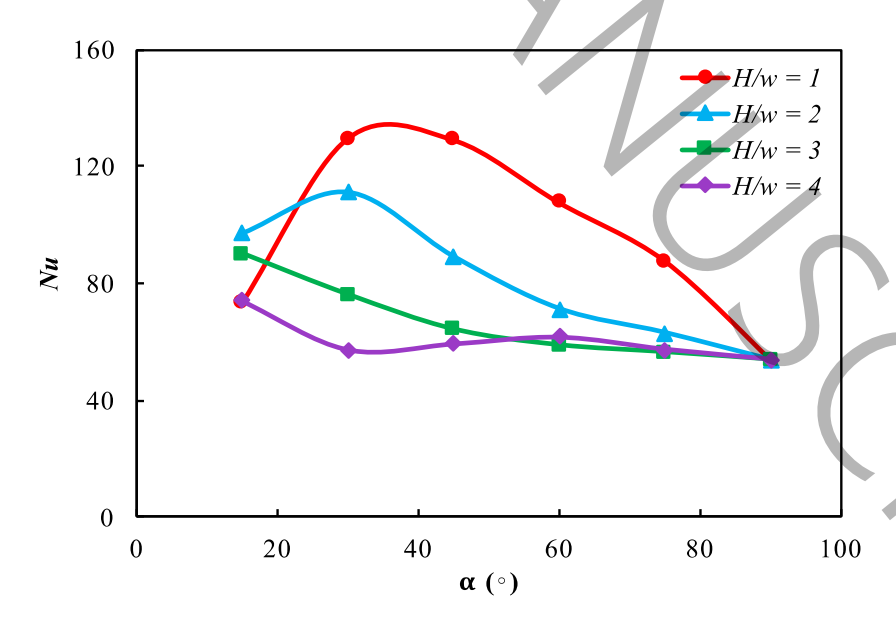


Fig. 6. Variation of Nu with angle of attack for different relative widths.

obstruction, maximizing shear stress and pressure loss. At very high angles, extensive flow separation creates larger, more stable recirculation zones that reduce shear stress gradient, slightly lowering the friction factor. Fig. 7 shows that f systematically decreases with the relative width. Multiple ribs promote more frequent but less intense flow disruptions, allowing for partial reattachment between ribs. This distributes and smooths the velocity profile, reducing localized high-shear regions and leading to a lower overall friction factor compared to a configuration with a single, highly obstructive rib.

Fig. 8 presents the variation of *THPP* with angle of attack for different relative widths, where *THPP* is defined by:

$$THPP = \frac{\left(Nu / Nu_s\right)}{\left(f / f_s\right)^{1/3}} \tag{13}$$

where Nu_s and Nu indicate the Nusselt number of the smooth and rough ducts and f_s and f signify the friction factor of the smooth and rough channels. This parameter represents the trade-off between heat transfer enhancement and friction penalty, providing a comprehensive measure of system efficiency. It can be seen in Fig. 8 that for relative width of 1, THPP increases from 15° to 30° due to the significant Nu

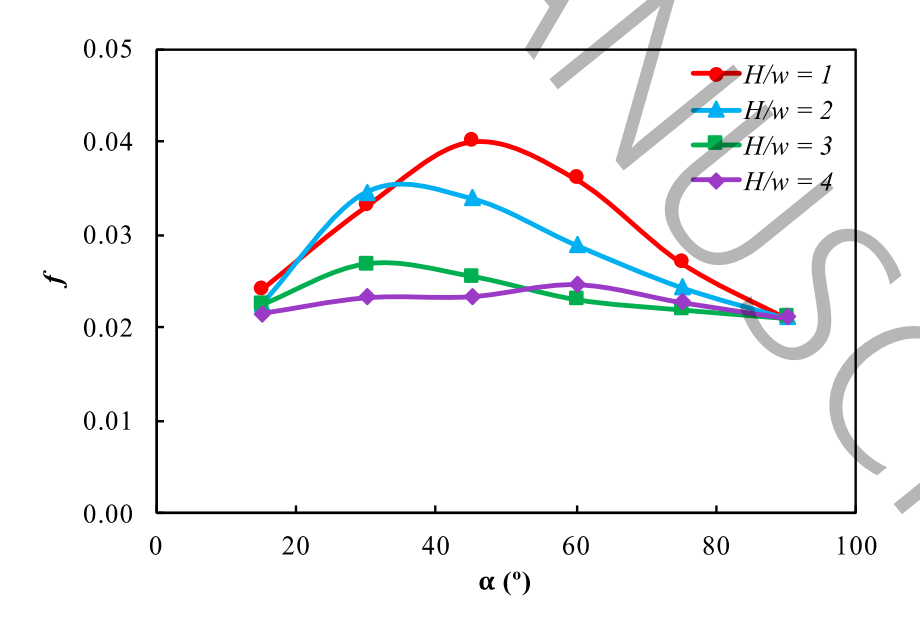


Fig. 7. Variation of f with angle of attack for different relative widths.

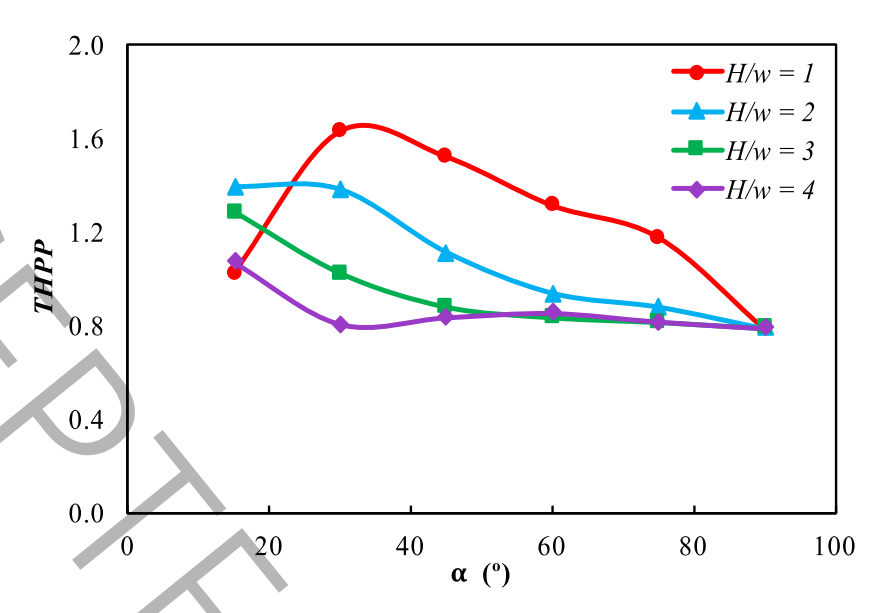


Fig. 8. Variation of *THPP* with angle of attack for different relative widths.

improvement outweighing f increase. THPP is maximum at 30° where best compromise between heat transfer and pressure drop happens. For large values of the relative width, the maximum THPP happens at 15° where early flow interference between ribs modifies optimal conditions.

This analysis provides critical insights for optimizing ribbed channel designs in practical applications where both thermal and hydraulic performance must be considered simultaneously.

Fig. 9 shows the variation of Nu and f for the configuration with the maximum THPP, namely an angle of attack of 30° and a relative width of 1. A comparison with the smooth duct results presented in Fig. 5 reveals that both Nu and f increase consistently across all Reynolds numbers, with a nearly uniform enhancement ratio observed throughout the tested range.

Velocity contours on a plane located 3 mm below the absorber plate are presented in Fig. 10 for four distinct geometric configurations, including (a) α =30° and H/W=1, (b) α =75° and H/W=1, c) α =30° and H/W=4, and (d) α =75° and H/W=4. Comparison between Figs. 10(a) and 10(b), as well as 10(c) and 10(d), highlights the influence of the angle of attack on flow behavior. At α =30° the flow exhibits higher velocity gradients near the apex of the V-rib, indicating strong local acceleration and the formation of secondary flow

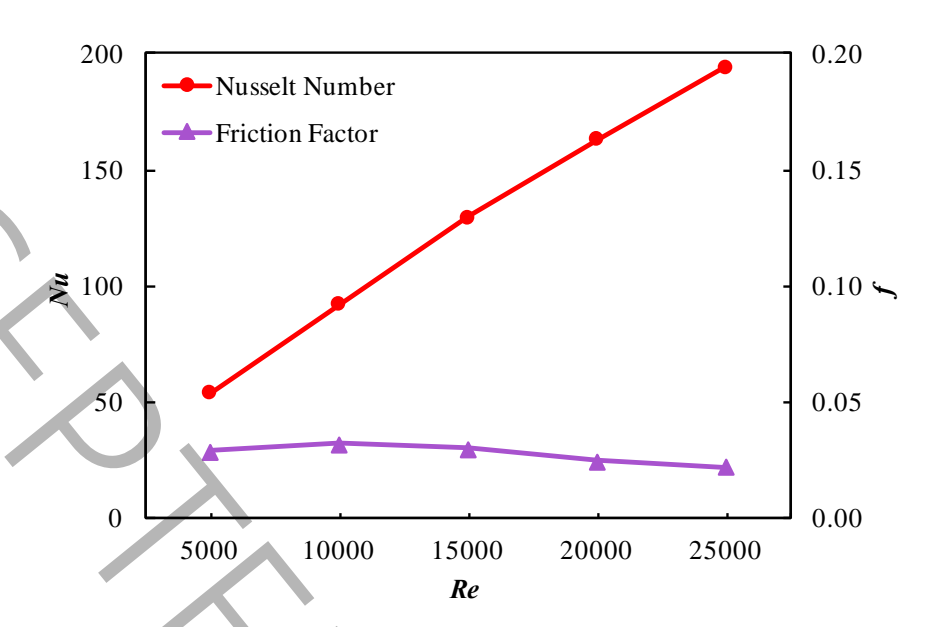


Fig. 9. Variation of Nu and f with Re for the angle of attack of 30° and relative width of 1.

structures. In contrast, at α =75°, the velocity distribution becomes more uniform, with reduced flow acceleration near the rib, suggesting weaker secondary motion and less pronounced flow separation. Furthermore, the results indicate that increasing the relative width, which corresponds to using a larger number of narrower V-ribs, reduces the strength and coherence of the secondary flows. This is because narrower ribs produce smaller, and less organized vortical structures that dissipate energy more quickly, resulting in lower overall secondary flow intensity compared to configurations with wider ribs.

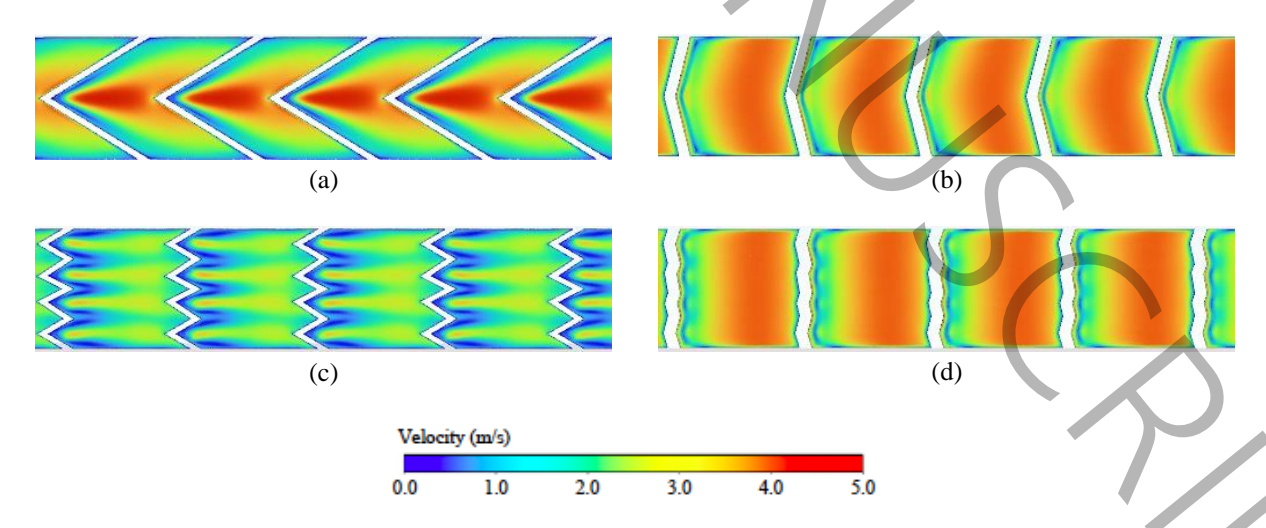


Fig. 10. Velocity contours on a plane located 3 mm below the absorber plate for a) α =30° and H/W=1 b) α =75° and H/W=1, c) α =30° and H/W=4, and d) α =75° and H/W=4.

Fig. 11 illustrates the temperature contours for the same cases as Fig. 10. A low angle of attack, which generates strong secondary flows and high-velocity jets, manifests on the temperature contours as intense, localized cool spots at the rib apex where heat removal is most efficient. However, this same flow structure creates large, adjacent recirculation zones visible as extensive areas of elevated temperature behind the ribs, where low velocity and long fluid residence time lead to poor heat transfer. In contrast, a high relative rib width, meaning a greater number of narrower ribs, alters this pattern significantly on the contours. Instead of a few large hot and cold zones, the temperature field shows a more fragmented and uniform distribution. Fig. 12 displays pressure contours on a vertical mid-plane along the channel for the same cases as Fig. 10. The contours confirm that pressure decreases progressively as flow passes the roughness elements, with the steepest gradient observed upstream of the ribs due to flow acceleration and obstruction. The pressure loss is most pronounced in Fig. 12(a), which exhibits the strongest flow disruption and highest bydraulic

The contours confirm that pressure decreases progressively as flow passes the roughness elements, with the steepest gradient observed upstream of the ribs due to flow acceleration and obstruction. The pressure loss is most pronounced in Fig. 12(a), which exhibits the strongest flow disruption and highest hydraulic resistance. In contrast, Fig. 12(c) shows the mildest pressure drop, indicating reduced flow disturbance. Figs. 12(b) and 12(d) result in nearly identical pressure losses, suggesting comparable aerodynamic resistance despite potential differences in rib geometry. These visual pressure patterns align quantitatively with the friction factor values reported in Fig. 7, where a higher-pressure gradient corresponds directly to a

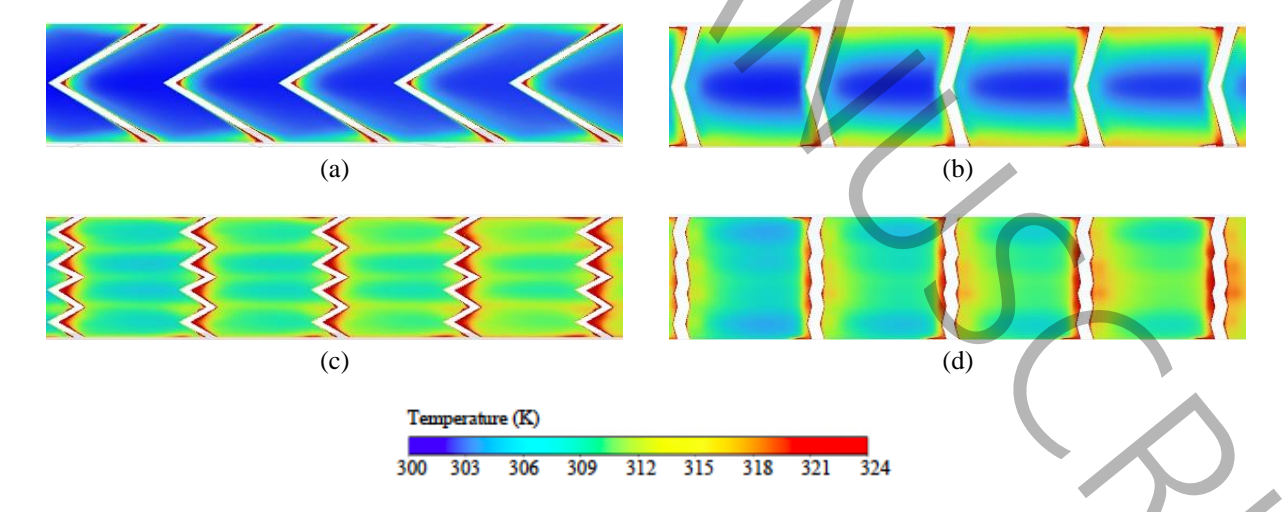


Fig. 11. Temperature contours on a plane located 3 mm below the absorber plate for a) α =30° and H/W=1 b) α =75° and H/W=1, c) α =30° and H/W=4, and d) α =75° and H/W=4.

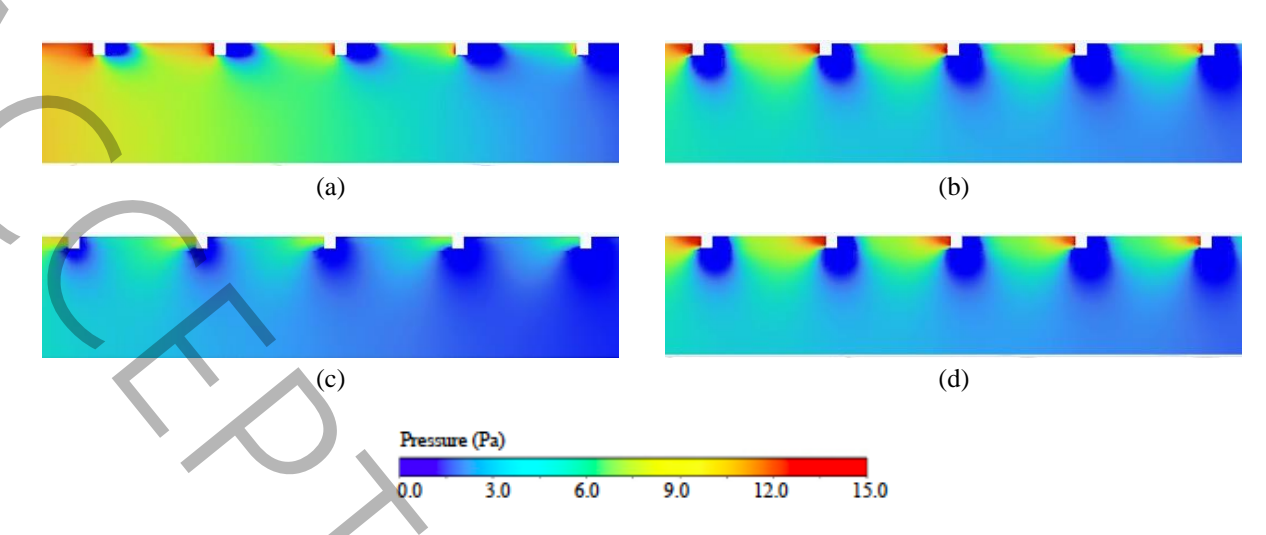


Fig. 12. Pressure contours on a vertical mid-plane along the channel for a) α =30° and H/W=1, b) α =75° and H/W=1, c) α =30° and H/W=4, and d) α =75° and H/W=4.

larger friction factor. This consistency confirms that the V-rib at low angle of attack and full width generates the greatest pressure loss, while other configurations yield comparatively lower flow resistance.

4. Conclusion

This study computationally investigates the thermo-hydraulic performance of a solar air heater duct roughened with V-shaped ribs, with particular focus on the simultaneous effects of angle of attack and relative rib width. Numerical results reveal distinct optimal configurations depending on rib arrangement. A single V-rib with a relative width of 1 achieves maximum performance at a 30° angle of attack, where strong vortex generation enhances thermal mixing without disproportionate pressure loss. At this optimum configuration, the Nusselt number reaches 2.8 times that of a smooth duct, with a thermo-hydraulic performance parameter of 1.63. Beyond 30°, increased flow separation reduces thermal efficiency. In contrast, configurations with larger relative widths perform optimally at a lower 15° angle of attack, as higher angles cause disruptive flow interference and increased friction. For practical applications, a relative width of 1 at 30° is recommended for maximum heat transfer, while systems sensitive to pressure drop may benefit from relative width of 2-3 at angle of attack of 15°. Beyond relative width of 4, diminishing returns in heat transfer do not justify the additional flow losses, making further rib additions impractical.

5. Nomenclature

f Friction factor

H Channel side length

k Turbulent kinetic energy

Nu Nusselt number

 \bar{P} Time-averaged pressure

Pr Prandtl number

 Pr_T Turbulent Prandtl number

wall heat flux

Re Reynolds number

 \overline{S}_{ij} Time-averaged strain rate tensor

 \overline{T} Time-averaged temperature

T' Temperature fluctuation

 $-\overline{T'u}$ Turbulent heat flux

 \overline{u}_i Time-averaged velocity component in the i direction

 u_i Velocity fluctuation

V Average flow velocity

w Width of a single V-rib

-u Reynolds stress

 x_i Position

Greek Letters

 α Thermal diffusivity

 $\delta_{::}$ Kronecker delta

v Kinematic viscosity

 V_{T} Turbulent eddy viscosity

 ρ Density

6. References

[1] R. Chauhan, N.S. Thakur, Investigation of the thermohydraulic performance of impinging jet solar air heater, Energy, 68 (2014) 255-261.

[2] S. Yadav, R.P. Saini, Numerical investigation on the performance of a solar air heater using jet impingement with absorber plate, Solar Energy, 208 (2020) 236-248.

[3] S. Yadav, R.P. Saini, K.M. Pandey, Effect of jet angle and jet pitch on the Thermo-Hydraulic performance of solar air heater having absorber plate with jet impingement, Thermal Science and Engineering Progress, 45 (2023) 102146.

[4] L.N. Azadani, N. Gharouni, Multi objective optimization of cylindrical shape roughness parameters in a solar air heater, Renewable Energy, 179 (2021) 1156-1168.

[5] H. Singh, C. Kishore, S. Chamoli, A. Joshi, Enhancing heat transfer in rectangular solar air heater channels: a numerical exploration of multiple Boomerang-shaped roughness elements with variable gaps, Energy Sources, Part A: Recovery, Utilization, and Environmental Effects, 46(1) (2024) 6696-6712.

[6] S.L. Sharma, K. Kishor, V.S. Bisht, A. Debbarma, A. Gaur, CFD analysis of artificially roughened solar air heater: a comparative study of C-Shape, reverse C-Shape, and reverse R-Shape roughness element, International Journal of Ambient Energy, 45(1) (2024) 2331240.

[7] A. Taghavi, A.H. Aghdam, Thermo-hydrodynamic analysis of various curved solar air-heaters with boot-shaped ribs: CFD simulations coupled with an optimized Artificial Neural Network model, Applied Thermal Engineering, 267 (2025) 125750.

- [8] A.M.E Momin, J.S. Saini, S.C. Solanki, Heat transfer and friction in solar air heater duct with V-shaped rib roughness on absorber plate, International Journal of Heat and Mass Transfer, 45(16) (2002) 3383–3396.
- [9] A. Lanjewar, J.L. Bhagoria, R.M. Sarviya, Heat transfer and friction in solar air heater duct with W-shaped rib roughness on absorber plate, Energy, 36(7) (2011) 4531-4541.
- [10] A. Lanjewar, J.L. Bhagoria, R.M. Sarviya, Experimental study of augmented heat transfer and friction in solar air heater with different orientations of W-Rib roughness, Experimental Thermal and Fluid Science, 35(6) (2011) 986-995.
- [11] A. Sharma, V. Goel, P. Kumar, G. Bharadwaj, Heat transfer and friction characteristics of double pass solar air heater having V-shaped roughness on the absorber plate, Journal of Renewable and Sustainable Energy, 5(2) (2013) 023109.
- [12] D. Jin, M. Zhang, P. Wang, S. Xu, Numerical investigation of heat transfer and fluid flow in a solar air heater duct with multi V-shaped ribs on the absorber plate, Energy, 89 (2015) 178-190.
- [13] D. Jin, S. Quan, J. Zuo, S. Xu, Numerical investigation of heat transfer enhancement in a solar air heater roughened by multiple V-shaped ribs, Renewable Energy, 134 (2019) 78-88.
- [14] M. Sharma, M. Bhargva, CFD based performance analysis of solar air heater provided with artificial roughness in the form of V Shaped ribs, Materials Today: Proceedings, 63 (2022) 595-601.
- [15] O. Nouri Kadijani, H. Kazemi Moghadam, S. Mousavi Ajarostaghi, A. Asadi, M. Saffari Pour, Hydrothermal performance of humid air flow in a rectangular solar air heater equipped with V-shaped ribs, Energy Science & Engineering, 10 (2022) 2276-2289.
- [16] N. Salarpour, L.N. Azadani, Optimization and evaluation of thermo-hydraulic performance of solar air heaters equipped with different roughness geometries, Case Studies in Thermal Engineering, 61 (2024) 105037.
- [17] H. Pachori, T. Choudhary, T. Sheorey, A. Kumar Shukla, V. Verma, A novel energy, exergy and sustainability analysis of a decentralized solar air heater integrated with V-shaped artificial roughness for solar thermal application, Sustainable Energy Technologies and Assessments, 66 (2024) 103816.

- [18] S.G. Noureini, L.N. Azadani, Thermal performance enhancement of a solar air heater with different roughness layouts, Case Studies in Thermal Engineering, 74 (2025) 106776.
- [19] R. Kumar, A. Kumar, R. Chauhan, M. Sethi, Heat transfer enhancement in solar air channel with broken multiple V-type baffle, Case Studies in Thermal Engineering, 8 (2016) 187-197.
- [20] R. Kumar, R. Chauhan, M. Sethi, A. Kumar, Experimental study and correlation development for Nusselt number and friction factor for discretized broken V-pattern baffle solar air channel, Experimental Thermal and Fluid Science, 81 (2017) 56-75.
- [21] R. Agrawal, R. Prasad, Thermal performance analysis of triangular solar air heater duct having broken V-shaped ribs, International Journal of Ambient Energy, 45(1) (2024) 2260814.
- [22] D. Jin, J. Zuo, S. Quan, S. Xu, H. Gao, Thermohydraulic performance of solar air heater with staggered multiple V-shaped ribs on the absorber plate, Energy, 127 (2017) 68-77.
- [23] A.K. Hegde, R. Pai, K.V. Karanth, Influence of solar insolation on energy and exergy efficiency of a rectangular duct solar air heater with various types of V rib roughness: An analytical approach, International Communications in Heat and Mass Transfer, 153 (2024) 107397.
- [24] D. Wilcox, Turbulence Modeling for CFD (Third Edition), DCW industries, 2006.
- [25] A.S. Yadav, J.L. Bhagoria, A CFD (computational fluid dynamics) based heat transfer and fluid flow analysis of a solar air heater provided with circular transverse wire rib roughness on the absorber plate, Energy, 55 (2013) 1127-1142.
- [26] ASHRAE, Methods of testing to determine the thermal performance of solar collectors, (2010).
- [27] B.R. Munson, T.H. Okiishi, W.W. Huebsch, A. P. Rothmayer, Fundamentals Of Fluid Mechanics 7th Edition, John Wiley and Sons, 2012.
- [28] F.W. Dittus, L.M.K. Boelter, Heat transfer in automobile radiators of the tubular type, International Communications in Heat and Mass Transfer, 12 (1) (1985) 3-22.